Applied Clay Science 254 (2024) 107372

Contents lists available at ScienceDirect

Applied Clay Science

journal homepage: www.elsevier.com/locate/clay

Research Paper

# Pressure-induced structural modifications of imogolite nanotubes and of their methylated analogues

Stéphan Rouzière [a,*], Victor Balédent [a,*], Jennifer Bodin [a], Erik Elkaim [b], Erwan Paineau [a], Pascale Launois [a]

[a] Université Paris Saclay, CNRS, Laboratoire de Physique des Solides, 1 rue Nicolas Appert, Orsay 91405, France
[b] Synchrotron SOLEIL, L'Orme des Merisiers, Saint-Aubin 91190, France

ARTICLE INFO

*Keywords:*
Imogolite
Nanotubes
Structure
Pressure
X-ray scattering
Young's modulus

ABSTRACT

Structural modifications of single-walled aluminosilicate clay nanotubes have been studied under hydrostatic pressure by in situ synchrotron X-ray scattering. Imogolite nanotubes (INT) of nominal composition $(OH)_3Al_2O_3SiOH$, and methyl-modified imogolite nanotubes (*m*-INT), $(OH)_3Al_2O_3SiCH_3$, have hydrophilic and hydrophobic internal cavities, respectively. Nanotube chiralities also differ, with zigzag (INT) and armchair (*m*-INT) chirality. In this work, pressure-induced changes in nanotube morphology and atomic structure are studied as a function of chirality, affinity of the inner cavity, and the pressure-transmitting medium used. Radial deformation and collapse of nanotubes are evidenced below 3 GPa, followed by the formation of a lamellar phase at higher pressures. In the case of INT, the collapse pressure value depends on the pressure transmitting medium chosen. Axial compressibility is measured, and a pseudo Young's modulus $Y$ is determined to be equal to ~265 GPa for INT and below 80 GPa for *m*-INT, underpinning the role of nanotube chirality in mechanical properties.

## 1. Introduction

Imogolite (INT) are single-walled aluminosilicate clay nanotubes of chemical formula $(OH)_3Al_2O_3SiOH$, naturally present in volcanic ash soils, as first discovered in 1962 in Japan (Yoshinaga and Aomine, 1962). A structural model was proposed by Cradwick et al. (1972), and the atomic structure determination was completed very recently (D'Angelo et al., 2023). What makes these structures unique is the way the silicon tetrahedra are arranged in the imogolite nanotube. Unlike other clay minerals, isolated tetrahedral $[(OH)SiO_3]$ units are linked by three mutual oxygen atoms to a rolled gibbsite-like layer of octahedral $[O_3Al(OH)_3]$ units (Fig. 1). The dangling hydroxyl group at the apex of tetrahedral sites makes the nanotube inner cavity highly hydrophilic. Remarkably, INT present a narrow distribution of diameters due to a well-defined, chirality-dependent, minimum of the strain energy needed to bend the gibbsite-like layer in order to give the tubular form (Konduri et al., 2006; Guimaraes et al., 2007; Lee et al., 2011). In this respect, they stand out from carbon nanotubes where the strain energy decreases monotonically with increasing diameters, and from the other mineral clay nanotubes, halloysite (Bates et al., 1950) and chrysotile (Whittaker, 1956; Krasilin, 2020), which are polydisperse and multi-walled scrolled nanotubes with much larger inner diameters than imogolite nanotubes. Due to their unique structural properties, imogolite nanotubes offer numerous potential applications in nanotechnology (Serra et al., 2019), including selective molecular sieving (Kang et al., 2014), gas storage (Zanzottera et al., 2012a) and photocatalysis (Elliott et al., 2017; Monet et al., 2020; Patra et al., 2023; Jimenéz-Calvo et al., 2023).

An important development was the successful synthesis of INT reported as early as 1977 (Farmer et al., 1977) using low-temperature solution-phase chemistry methods (Farmer and Fraser, 1979). Later, several groups proposed the possibility to synthesize analogues of INT by isomorphic substitution of silicon by germanium (Wada and Wada, 1982; Mukherjee et al., 2005; Ookawa et al., 2006). It was shown that the nanotube diameter can be controlled by finely-tuning the degree of substitution (Konduri et al., 2007; Thill et al., 2012). Substitution with germanium also produces single or double-walled nanotubes (Maillet et al., 2010; Amara et al., 2013). In addition, the INT's inner surface can be functionalized by replacing hydroxyl groups with methyl groups, making its cavity hydrophobic (Bottero et al., 2011; Amara et al., 2015). Interestingly, the functionalization of the inner cavity also induces a change in the nanotube chirality (i.e. the way how the tube rolls itself) as evidenced from the determination of the atomic structure based on

---

* Corresponding authors.
*E-mail addresses:* stephan.rouziere@universite-paris-saclay.fr (S. Rouzière), victor.baledent@universite-paris-saclay.fr (V. Balédent).

https://doi.org/10.1016/j.clay.2024.107372
Received 5 January 2024; Received in revised form 3 April 2024; Accepted 8 April 2024

observed periodicity peaks 00*l* (Monet et al., 2018). It may be mentioned that Park et al. (2014) proposed earlier an armchair structure for methylated imogolites but it was based on a wrong analysis of their X-ray scattering diagram; the interested reader can refer to Monet et al. (2018) for more information.

The structure of INT and *m*-INT can be labeled by two integers (N,M) (Guimaraes et al., 2007), the components of the so-called "chiral vector" in the hexagonal lattice based on the $(OH)_3Al_2O_3Si(OH/CH_3)$ elementary unit, describing the rolling mode of the nanotube (Monet et al., 2018). By analogy with single-walled carbon nanotubes (Robertson et al., 1992), *m*-INT has an "armchair" (AC) arrangement with chiral vector (9,9) and a period $T \simeq 4.89$ Å along the tube axis (Monet et al., 2018), while INT has a "zigzag" (ZZ) arrangement, our sample containing a mixture of 50% (13,0) and 50% (14,0) chiral vectors with a period $T \simeq 8.40$ Å (D'Angelo et al., 2023). Radial dimensions of INT and *m*-INT analogues are quite similar (see Table 1). Moreover, INT have been shown to assemble into small bundles formed of ~19 tubes approximatively, which organize themselves on a two-dimensional (2D) hexagonal lattice in the plane perpendicular to the tube axis (D'Angelo et al., 2023). It should be noted that nanotubes lose their perfectly cylindrical shape in the dry state compared to the suspension, due to their aggregation into bundles during the drying (D'Angelo et al., 2023).

The application of an external stimulus such as the pressure is expected to modify the structural, electric and mechanical properties of nanotubes, or to provide the basis of new nanomaterials induced, for instance, by polygonization or polymerization as shown for carbon nanotubes (San Miguel, 2006). However, very few experimental works have investigated the effect of pressure on clay mineral nanotubes. Zhang et al. (2018) evidenced that compression induced a lattice distortion as well as modulations of electrical transport properties in iron doped chrysotile nanotubes. We recently reported the first experimental investigation on the compressibility and structural modifications of synthetic aluminogermanate imogolite-like nanotubes (Ge-INT) under hydrostatic pressure (Rouzière et al., 2023). Meanwhile, computational studies reported that the calculated Young's modulus of aluminosilicate INT ranges from 100 to 400 GPa (Guimaraes et al., 2007; Li et al., 2008; Teobaldi et al., 2009; Lourenço et al., 2014; Liou et al., 2015; Chagas da Silva et al., 2015; Gonzalez et al., 2016), such values being comparable to those of halloysite and chrysotile nanotubes (Piperno et al., 2007; Lecouvet et al., 2013; Pebdani, 2023). But to date, no experimental work has been carried out on imogolite nanotubes under pressure. In the present study, we investigate the structural modifications under pressure of synthetic (INT, hydrophilic) and methylated (*m*-INT, hydrophobic) imogolite nanotubes by performing in situ synchrotron X-ray scattering experiments, using a diamond anvil pressure cell. Pressure-induced radial deformations up to nanotube collapse are measured, as is axial compressibility. The role of the nanotube chirality on the nanotube axial compression is highlighted. We also evaluate the effect of two different pressure transmitting media (PTM), silicone oil and an alcohol mixture, in relation to the diameter and affinity of the inner nanotube cavity.

**Table 1**
Inner $R_i$ and outer $R_o$ radii, radial collapse pressure $P_c$ depending on the PTM used (Si oil or meth/eth mixture), and the pseudo Young's modulus $Y$, of synthetic and methylated alumino-silicate and germanate imogolite nanotubes. Symbols indicate values obtained from the literature (* Amara et al. (2014); † Monet et al. (2018); ‡ D'Angelo et al. (2023); § Rouzière et al. (2023)).

| Type | $R_i$-$R_o$ (Å) | $P_c^{Si-oil}$ (GPa) | $P_c^{meth/eth}$ (GPa) | Chirality | $Y$ (GPa) |
|---|---|---|---|---|---|
| INT (13,0) + INT (14,0) | 7.4–11.7$^{\ddagger}$<br>8.1–12.5$^{\ddagger}$ | 2.0 ± 0.4 | 2.8 ± 0.4 | ZZ | 265 ± 10 |
| *m*-INT | 8.8–13.6$^{\dagger}$ | 2.4 ± 0.2 | 2.4 ± 0.2 | AC | ≤ 80 |
| Ge-INT | 13.8–20.3* | 1.4 ± 0.2 | 2.6 ± 0.2 | ZZ | 400 ± 10$^{\S}$ |
| *m*-Ge-INT | 11.6–16.2$^{\dagger}$ | 3.7 ± 0.2 | 4.4 ± 0.6 | AC | 200 ± 20$^{\S}$ |

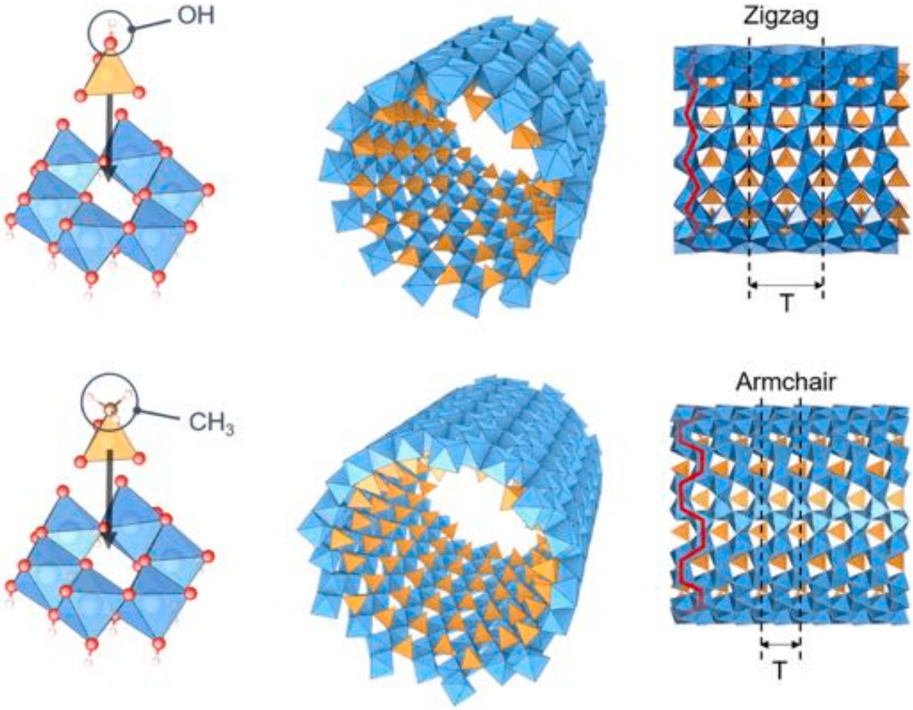

**Fig. 1.** Structure of INT (13,0) (top) and *m*-INT (9,9) (bottom). Zigzag (INT) and armchair (*m*-INT) chiralities are indicated by the red lines, and the corresponding periods *T* are also shown. (For interpretation of the references to colour in this figure legend, the reader is referred to the web version of this article.)

## 2. Material and methods

### 2.1. Sample description

Synthetic imogolite nanotubes (INT) were obtained through a process involving a solution containing tetraethoxy orthosilicate (TEOS), $AlCl_3(H_2O)$ and NaOH. Following hydrothermal treatment, the resulting suspension was purified by diafiltration with ultrapure water and concentrated by ultrafiltration, as detailed in Belorizky et al. (2010). To synthesize methylated imogolite nanotubes (*m*-INT), TEOS was replaced by a methyltriethoxysilane (MTES) agent in presence of aluminum perchlorate and NaOH, following the procedure described elsewhere (Amara et al., 2015). After recovering the suspensions, all samples were dialyzed against ultrapure water, using 8 kDa membranes in order to remove residual salts and alcohol in excess. Dialyses were performed until the conductivity dropped below 5 $\mu S.cm^{-1}$. Purified suspensions were dried at 70 °C to yield a thin film, which was subsequently crushed and sifted through a 100 μm mesh grid, to obtain a fine powder. The dried powders used for X-ray scattering measurements were heated at 200 °C at ambient pressure for 2 h, in order to remove all water from the sample (Liao et al., 2018; D'Angelo et al., 2023).

The purity of the samples was assessed by a careful analysis of X-ray scattering diagrams (Monet et al., 2018; D'Angelo et al., 2023) and by Fourier transform infrared (FT-IR) spectroscopy (Fig. S1). The comparison of FTIR curves confirms the replacement of hydroxyl groups by methyl groups as evidenced by the appearance of the characteristic stretching $\nu$ (2978 and 2920 $cm^{-1}$) and bending $\delta$ (1275 $cm^{-1}$) modes of $CH_3$ groups and the absorption band at 780 $cm^{-1}$ related to the Si—C stretching vibration (Amara et al., 2015). The doublet characteristic of the imogolite nanotube structure is found at 990/940 $cm^{-1}$ for INT and 960/910 $cm^{-1}$ for *m*-INT, in good agreement with previous observations (Amara et al., 2015). Finally, the modes below 700 $cm^{-1}$ are mainly due to Al—O stretching modes linked to the imogolite-type structure (Bishop et al., 2011; Amara et al., 2015).

### 2.2. X-ray scattering experiments

X-ray scattering (XRS) measurements under pressure were carried out on a two-circle powder diffractometer equipped with silicon-strip linear detectors (Mythen2, Dectris) on the CRISTAL beamline at Synchrotron SOLEIL (Saint Aubin, France). Powder diagrams extend over the $Q$ scattering wavevectors range, 0.1 to 5 $Å^{-1}$, with beam wavelength $\lambda = 0.72844$ Å ($Q = \frac{4\pi}{\lambda} sin\theta$, $2\theta$ being the scattering angle).

XRS measurements of dried powders at ambient pressure were performed on an X-ray copper (Cu) rotating anode generator (Rigaku, HU3R) on the MORPHEUS platform at Laboratoire de Physique des Solides (LPS). The monochromatized X-ray beam (wavelength, $\lambda_{CuK\alpha} = 1.5418$ Å) was collimated by parabolic confocal W/Si multilayers mirrors (Osmic, Inc.). Powders were filled into borosilicate glass capillaries of 1 mm diameter (WJM-Glas, Müller GmbH). XRS patterns were collected on a two-dimensional large-area detector (MAR345, marXperts GmbH) with 150 μm pixel size, the sample to detector distance being fixed to 250 mm. The intensity as a function of the wavevector $Q$ was obtained by angular integration of the two-dimensional pattern using a home-made software. Geometric and polarization corrections together with correction for air adsorption between the sample and the detector were applied to the data.

X-ray scattering is a powerful and nondestructive technique to characterize imogolite nanotubes (Maillet et al., 2010; Amara et al., 2014, 2015; Monet et al., 2018; D'Angelo et al., 2023). Typical XRS diagrams from dried powders are shown in Fig. 2. The observed broad modulations reflect the finite radial nanometric dimension of the tubes, radial dimensions and cross-sectional shape of the nanotube being described by the modulations below $Q < 1$ $Å^{-1}$ (Amara et al., 2014, 2015; D'Angelo et al., 2023). Additionally, these modulations also reflect the arrangement of nanotubes on the hexagonal 2D lattice in bundles. The average hexagonal lattice parameter and the number of tubes can be determined from the analysis of both position and width of the modulations labeled with the Miller indices (*h*,*k*) (Paineau et al., 2017). It was shown for INT that the average number of tubes per bundle is 19 (D'Angelo et al., 2023). The width of the 10 peak is similar between INT and *m*-INT diffractograms and these nanotubes have close radial dimensions. One can thus conclude that *m*-INT are also organized in bundles containing about 19 nanotubes. Finally, let us underline that the evolution of the modulations below $Q < 1$ $Å^{-1}$ as a function of pressure provides information on changes in nanotube morphology and organization. On the other hand, modulations at larger $Q$ values ($Q > 1$ $Å^{-1}$) yield the information on the nanotube structure at the atomic scale. In particular, the asymmetric ("sawtooth" shape) peak labeled 002, is associated with the period $T$ along the long tube axis, with $T = 4\pi/Q_{002}$. Note that the period value is determined by the inflexion point of the rising edge of the peak; the steeper the rising edge, the larger is the coherence length along the nanotube axis. The coherence length was previously determined to be equal to 200 Å for INT (D'Angelo et al., 2023) and 100 Å for *m*-INT (Monet et al., 2018). INT and *m*-INT having different chiralities and periods (Monet et al., 2018; D'Angelo et al., 2023), the 002 signature is located around 1.50 and 2.57 $Å^{-1}$ respectively (see Fig. 2).

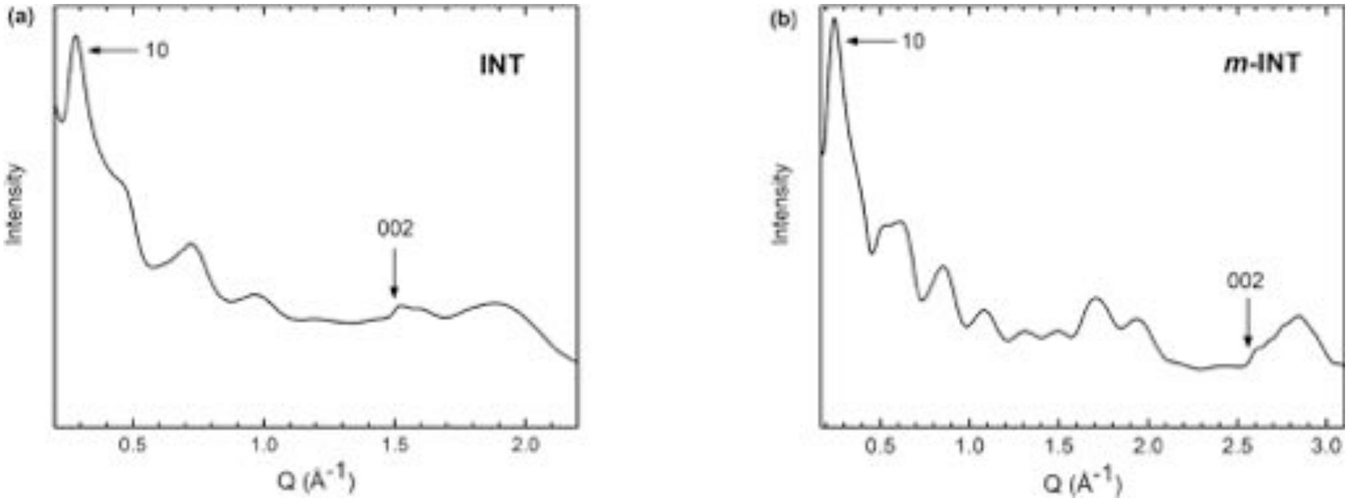

**Fig. 2.** XRS experimental diagrams of dried (a) INT and (b) *m*-INT powders. Arrows indicate the respective position of the 10 (2D hexagonal lattice) and 002 (axial periodicity) peaks for INT and *m*-INT. Intensity corrections are applied (see text) and curves are plotted with intensity in log scale.

### *2.3. Pressure measurements*

Pressure measurements were conducted using a diamond anvil cell (DAC) equipped with a 1 mm culet diamond. The powder sample was placed inside a copper-beryllium gasket with a hole of 500 μm diameter and 80 μm thickness. Loading the powder sample into the high-pressure cell takes place within 5 min after removal from the oven, while the sample is still hot. It is immediately covered with a transmitting medium before closing the cell.

To monitor the pressure, a ruby chip was used, and the pressure was determined via the ruby fluorescence calibration (Chijioke et al., 2005), with an uncertainty of approximately ±0.1 GPa. Two pressure transmitting media (PTM) were employed to achieve quasi-hydrostatic pressure below 8 GPa (Tateiwa and Haga, 2009). These PTM were silicone (Si) oil (Rhodorsil silicone oil 47 V 1000) and a methanol:ethanol (meth/eth) mixture in a 4:1 volumetric proportion. The pressure measurements were carried out by ramping up from ambient to the maximum pressure. Before and after each measurement, the ruby fluorescence line was examined to account for any pressure drift, resulting in an overall uncertainty of 5% of the pressure value: 0.1 at 1 GPa and 0.5 at 8 GPa. Due to the gasket shrinking and variations in the sample's thickness with increasing pressure, it was not possible to calibrate the intensity into absolute units for X-ray scattering patterns. Therefore, XRS patterns are presented in arbitrary intensity units.

It is worth noting that PDMS $(C_2H_6OSi)_n$ molecules (molecular weight of ~40,000 g/mol in Rhodorsil silicone oil 47 V 1000) are unsuitable for fitting inside the internal pore of INT because of their large gyration radius (Rg ≈ 5.6 nm) (Ma and Xu, 1994). On the other hand, ethanol ($C_2HO_5H$) or methanol ($CH_3OH$), with molecular size of 0.469 and 0.408 nm respectively (Marcus, 1998), are deemed suitable for this purpose.

## 3. Results and discussion

### *3.1. Nanotube radial compression and collapse*

XRS measurements of INT and *m*-INT under pressure with the two PTM are plotted in Fig. 3. Modulations located at $Q < 1$ Å$^{-1}$ are clearly observed at the lowest pressure, then progressively fade away as the pressure is increased. The variation in intensity is due to deformations of the cross-sectional nanotube shape, which increasingly deviates from the circular one through ovalization process. This behavior was also reported for single-walled aluminogermanate nanotubes Ge-INT (Rouzière et al., 2023). Meanwhile, the position of modulations does not vary under the effect of pressure. This indicates that no polygonization of INT and *m*-INT occurs, whereas hexagonalization of Ge-INT, arranged in much larger bundles (~ 60 tubes) though, was evidenced under pressure, with the decrease of the hexagonal lattice parameter reflecting the change in nanotube shape (Rouzière et al., 2023).

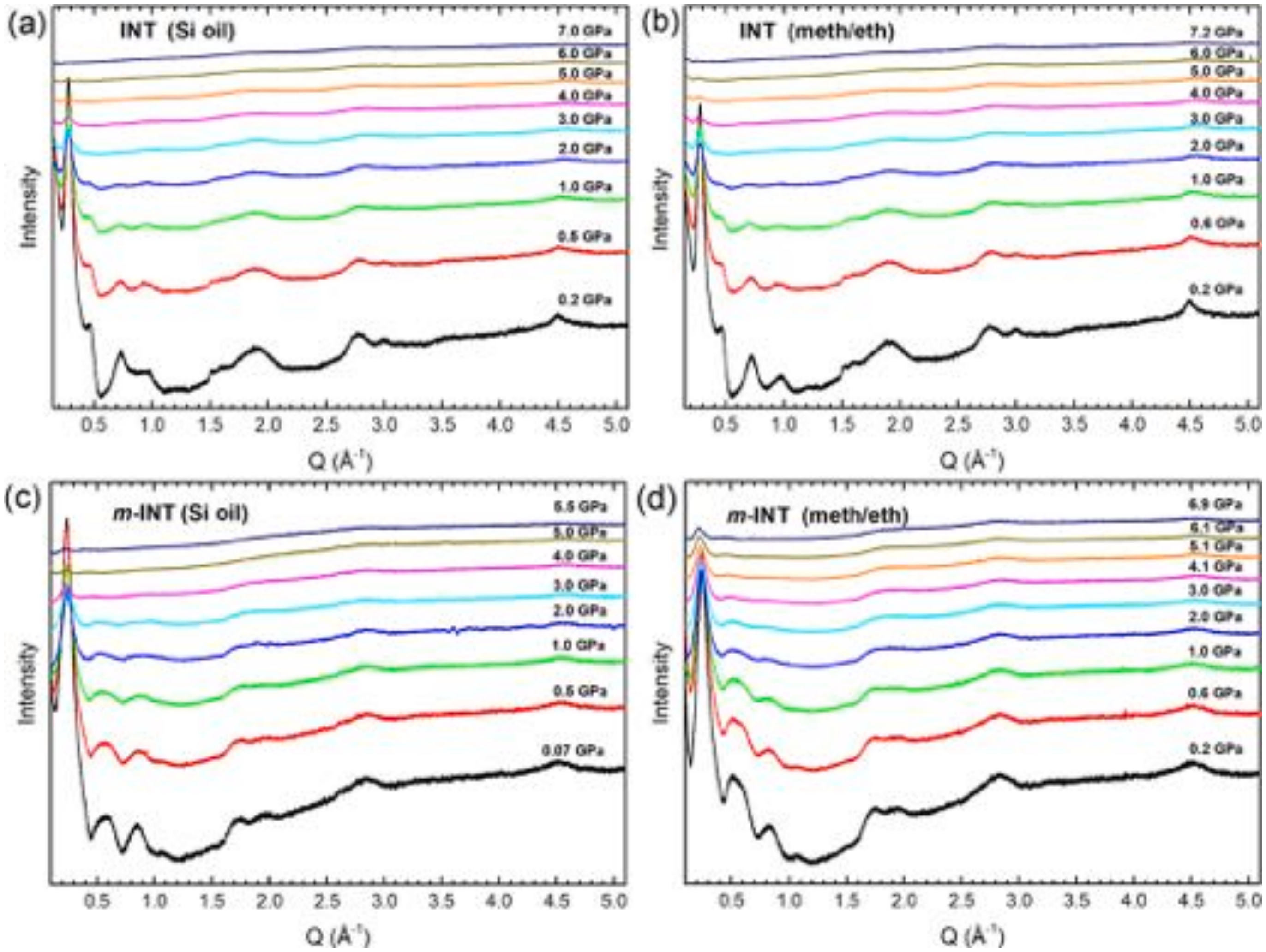

**Fig. 3.** XRS diagrams of INT (a, b) and *m*-INT (c, d) as a function of the pressure, with Si oil and methanol:ethanol (meth/eth) mixture PTM. Intensity is in log scale. Curves are vertically translated for the sake of clarity.

At low scattering wavevectors, the final disappearance of modulations corresponds to the radial collapse of the nanotube occurring at the collapse pressure $P_c$. Still, a small scattering peak remains present at higher pressures, located at $Q \sim 0.26$ Å$^{-1}$ for INT and 0.215 Å$^{-1}$ for *m*-INT, corresponding to a distance $d$ ($d = \frac{2\pi}{Q}$) of 2.4 and 2.9 nm respectively. It is reminiscent of the formation under pressure of a lamellar phase which was observed in methylated Ge-INT, with an interlayer distance of 3.6 nm (Rouzière et al., 2023), or the one issued from the thermal collapse of *m*-INT at 570 K (Zanzottera et al., 2012b), with an interlayer distance of 2.6 nm. As suggested by the authors of these earlier works, the mechanism of lamellar phase formation corresponds to the flattening of nanotubes after their collapse. Some partially collapsed INT present between patches of layers, may act as spacers to explain such a large $d$ distance. Indeed, it is worth noting that the variation in $d$ values and nanotube outer diameters (see Table 1) follows the same trend, being larger with the methylation or with the substitution of Si by Ge. In our study, lamellar-phase peak intensity decreases with increasing pressure, and disappears at the highest pressure ($P = 7$ GPa) for INT, while its intensity is strongly reduced for *m*-INT. High scattering harmonics associated with the lamellar phase cannot be observed either, apart from the second harmonic in *m*-INT with alcohol mixture PTM. This indicates a strong disorder in the lamellar phase, which becomes increasingly important as the intensity of the lamellar phase-related peaks decreases with increasing pressure.

To better characterize the onset of nanotube collapse, the evolution of the tubular shape is quantified by plotting the variation of the peak area of the third modulation as a function of the pressure (Fig. 4). The variation of the values is fitted with a Gaussian lineshape function, after substracting the background signal which is almost linear in this region. The empirical fitting function of the evolution of the modulation amplitude as a function of pressure simply writes:

$$I = I_0 exp(-P/P_a) \qquad (1)$$

Same $P_a$ values were determined for *m*-INT with both PTM ($P_a \sim 1.2$ GPa). However, the $P_a$ value is larger for INT with alcohol mixture as PTM ($P_a = 1.4$ GPa) than with Si oil ($P_a = 1.0$ GPa). This means a weaker deformation of INT as a function of pressure with alcohol PTM, which is attributed to the filling of the inner nanotube cavity by methanol and ethanol molecules, which limits the radial compression of the nanotube. The same effect was also observed in Ge-INT (Rouzière et al., 2023).

Moreover, the pressure $P_a$ determined by this fit is directly proportional to the radial collapse pressure $P_c$, defined as the pressure above which the oscillation amplitude hardly varies. Indeed, using this fitting function with the $P_c = 2P_a$ relation on Ge-INT data, we find the same trend for collapse pressure values as those reported in Rouzière et al. (2023), which corroborates our present analysis. The values of $P_c$ for INT and *m*-INT are reported in Table 1, together with the ones for standard and methylated Ge-INT. A larger collapse pressure is observed for INT and Ge-INT with the alcohol mixture PTM due to the filling of these hydrophilic nanotubes by ethanol and methanol molecules which makes them less radially deformable under pressure than with Si oil PTM. Conversely, the collapse pressure values for methylated nanotubes are the same with both PTM within error bars, meaning that the affinity of the internal cavity for alcohol molecules is much weaker in *m*-INT and *m*-Ge-INT than in INT and Ge-INT.

### 3.2. Nanotube axial compression

The compression along the nanotube axis can be evaluated by following the variation of the position of the inflexion point of the rising edge of (002) asymmetric peak. At the lowest pressures (Fig. 3), the asymmetric peak is observed for INT at $Q_{002} = 1.495$ Å$^{-1}$ with both PTM. It is only slightly noticeable for *m*-INT with Si-oil PTM at the position close to $Q_{002} = 2.57$ Å$^{-1}$, whereas it cannot be observed with the alcohol mixture PTM.

For INT, the $Q_{002}$ peak attenuates as pressure rises before disappearing at 4 GPa. The variation of the axial period ($T = 4\pi/Q_{002}$) as a function of the pressure is plotted in Fig. 5a. The period $T$ decreases linearly with the same slope for both PTM, seemingly comparable to that previously reported for Ge-INT (Rouzière et al., 2023). There is no effect of the tube filling by alcohol mixture PTM on axial compression, contrary to radial compression. The absence of the $Q_{002}$ peak at high pressures ($P > 3$ GPa) corresponds to the loss of long range order along the tube axis, and it is concomitant with the radial collapse of the nanotube. On the contrary, the loss of long range order occurs more rapidly in *m*-INT as the $Q_{002}$ peak disappears above 1 GPa with the Si-oil PTM while it cannot be observed with alcohol mixture PTM. The decrease of the axial period $T$ of *m*-INT as a function of the pressure with the Si-oil PTM is plotted in Fig. 5b. In comparison, the $Q_{002}$ peak was still measured after the nanotube radial collapse in Ge-INT and *m*-Ge-INT, describing the transition from a compression regime to a relaxation regime where the $T$ period increases (Rouzière et al., 2023). This was explained by the release of structural curvature-related constraints as the nanotube flattens during nanotube collapse, leading to the lamellar phase. This behavior is not observed for INT and *m*-INT, which indicates that the planar structure is more disrupted by the effect of pressure for these nanotubes. The absence of the compression-relaxation transition and the strong disorder in the lamellar phase, suggests that their structures are more fragile than those of Ge-based INT. This may be linked to the greater curvature of INT, because their inner diameter is smaller than that of Ge-INT (see Table 1): the transformation from a rolled structure

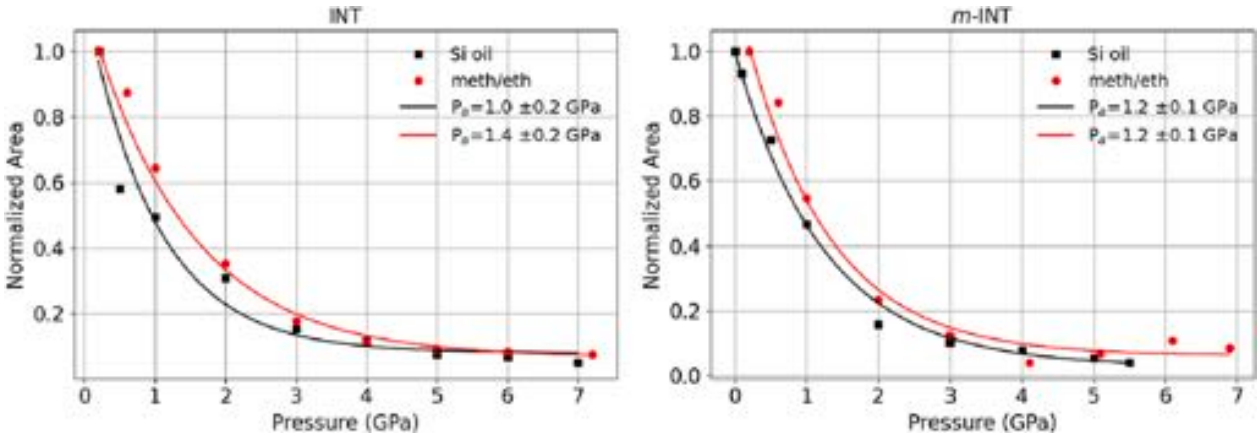

**Fig. 4.** Variation of the normalized area of the modulation located between 0.6 and 0.85 Å$^{-1}$ (resp. 0.7 to 1 Å$^{-1}$) for INT (resp. *m*-INT) as a function of pressure for both PTM. Lines correspond to the fitting curves of the experimental values (see text); the fit takes into account the uncertainty of 5% on the pressure values.

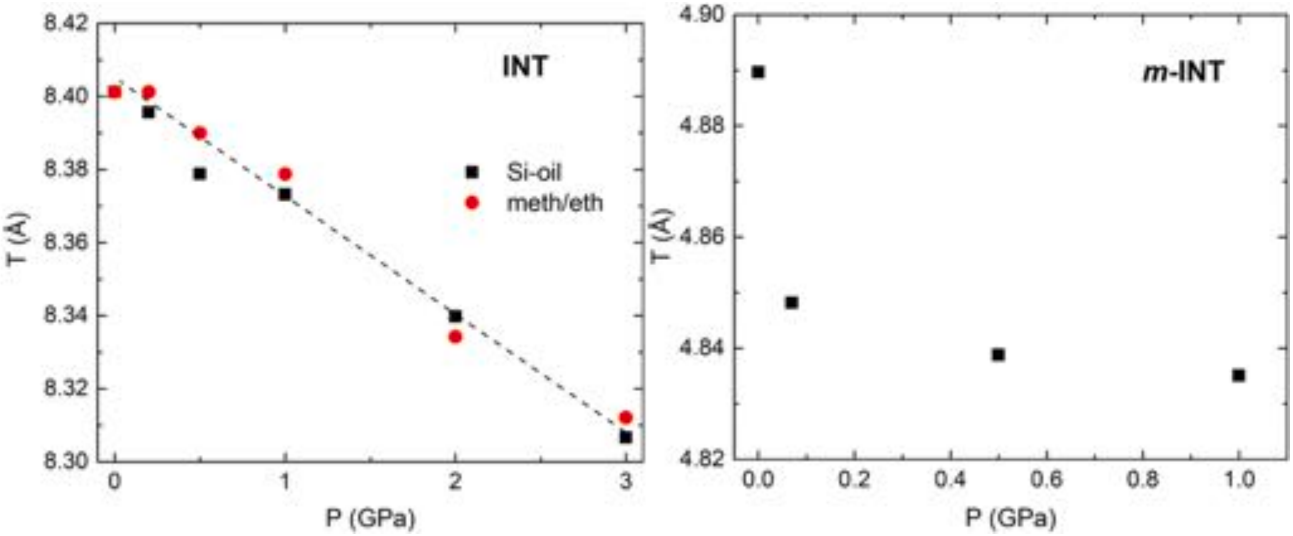

**Fig. 5.** Pressure-induced variation of the axial period $T$ of, (a) INT with Si-oil (squares) and alcohol mixture (circles) PTM, (b) *m*-INT with Si-oil PTM.

to a planar one leads to greater bond and angle distorsions.

As discussed in Rouzière et al. (2023), it is possible to derive a pseudo axial Young's modulus $Y$ from the linear variation of the period upon the pressure plotted in Fig. 5a, by neglecting the contribution from the shear modulus and the radial Young's modulus via the Poisson ratios. Indeed, by analogy with CNT, this approximation would give the correct order of magnitude, as the Poisson ratio is estimated to be around 0.1 (Chen et al., 2010) and the shear modulus is typically from 2 to 3 orders of magnitude lower than the Young's modulus (Salvetat et al., 1999). Young's modulus $Y$ is defined as $P = Y\frac{T_0 - T}{T_0}$ ($T_0$ is the period value at ambient pressure). Value found is $Y \sim 265$ GPa for INT. For *m*-INT, uncertainties on period values measured under pressure on very small intensity peaks make a linear fit of Fig. 5(b) difficult. One thus takes for $T_0$ the value of the period measured at ambient pressure and the value $T$ at 1 GPa. It gives an upper limit of the Young's modulus equal to 80 GPa as Young's modulus calculated in the same way from the period values at 0.07 GPa and 0.5 GPa are smaller. Pseudo Young's moduli of INT and *m*-INT are smaller than the ones previously determined for their Ge counterparts ($Y \sim 400$ GPa for Ge-INT and $Y \sim 200$ GPa for *m*-Ge-INT (Rouzière et al., 2023)), as reported in Table 1. Interestingly, $Y$ is smaller for the methylated analogues of INT and Ge-INT (Table 1). We can therefore infer that chirality plays a role in the value of the Young's modulus and in mechanical properties of the nanotubes, as the methylated analogues possess an armchair chirality different from the zigzag chirality of INT and Ge-INT.

To our knowledge, no theoretical value of the Young's modulus has been calculated for *m*-INT. However, there is some literature on calculating the mechanical properties of INT, in particular the axial Young's modulus, using various numerical methods. The density-functional tight-binding method, the most widely used, determines slightly different Young's moduli for INT similar to those used in this study, i.e. with (13,0) and (14,0) chiral indices. The earliest study found moduli of 255 and 290 GPa respectively (Guimaraes et al., 2007), to be compared to the measured value of 265 GPa. However, the authors report large discontinuous variations in this modulus as a function of tube diameter, without providing an explanation for this non-intuitive result. Other more recent studies using a similar method report a higher modulus of 360 GPa (Lourenço et al., 2014). The interested reader may also see references (Li et al., 2008; Teobaldi et al., 2009; Liou et al., 2015; Chagas da Silva et al., 2015; Gonzalez et al., 2016) for Young's moduli of nanotubes with different chiral indices than the ones studied in this article, using various density functional theory calculations, ab-initio calculations, molecular dynamics calculations or a continuum model. Put together, these articles reflect a wide dispersity in Young's modulus values. However, in light of these theoretical predictions, it is important to underline that in our study we are determining a pseudo Young's modulus. In fact, the stress applied here is not uniaxial but hydrostatic and therefore isotropic, which intuitively leads to an overestimation of Young's modulus. It would be interesting to calculate the axial contraction during isotropic compression. This would enable a more rigorous comparison between theory and experience. In addition, other parameters also come into play in determining Young's modulus, such as tube length (Liu and Kang, 2017) or defects (Liou et al., 2015). Despite all these reservations, our experimentally determined value is well within the range of calculated values.

## 4. Conclusions

Pressure-induced structural modifications of imogolite nanotubes and of their methylated analogues have been investigated by in situ X-ray scattering measurements. Results show that nanotubes undergo strong radial deformations until their final collapse, which occurs at $P_c \leq 3$ GPa. Moreover, concerning INT, the filling of the inner cavities by alcohol molecules of the pressure transmitting medium leads to a radial collapse at higher pressure than with silicon oil PTM. No difference in the collapse pressure value is observed for *m*-INT with the two PTMs, which may be linked to the lower affinity of the methylated inner cavity towards polar (alcohol) molecules. Above the collapse pressure, the strong structural change observed is reminiscent of the formation of a lamellar phase in both compounds. The axial compressibility measured is shown to be dependent on the nanotube chirality, with the determination of a pseudo Young's modulus equal to $Y \sim 265$ GPa for imogolite nanotubes of zigzag chirality, compared to $Y \leq 80$ GPa for their methylated analogues with armchair chirality. Our findings, together with those obtained previously on aluminogermanate imogolite-like nanotubes (Rouzière et al., 2023), should motivate further experimental and theoretical studies to foresight mechanical properties of these nanotubes in relation with their chirality.

## CRediT authorship contribution statement

**Stéphan Rouzière:** Writing – original draft, Methodology, Data curation, Conceptualization. **Victor Balédent:** Writing – review & editing, Methodology, Investigation, Data curation, Conceptualization. **Jennifer Bodin:** Investigation, Data curation. **Erik Elkaim:** Methodology, Investigation. **Erwan Paineau:** Writing – review & editing, Investigation. **Pascale Launois:** Writing – review & editing, Investigation, Data curation.

## Declaration of competing interest

The authors declare that they have no known competing financial interests or personal relationships that could have appeared to influence the work reported in this paper.

## Data availability

The authors are unable or have chosen not to specify which data has been used.

## Acknowledgements

We acknowledge the synchrotron SOLEIL for provision of beamtime on the CRISTAL beamline (proposal numbers 20191353 and 20110185). The authors thank P. Davidson for kindly providing the imogolite suspension for later drying.

## Appendix A. Supplementary data

Supplementary data to this article can be found online at https://doi.org/10.1016/j.clay.2024.107372.

## References

Amara, M.S., Paineau, E., Bacia-Verloop, M., Krapf, M.E.M., Davidson, P., Belloni, L., Levard, C., Rose, J., Launois, P., Thill, A., 2013. Single-step formation of micron long (oh)3al2o3ge(oh) imogolite-like nanotubes. Chem. Commun. 49, 11284–11286. https://doi.org/10.1039/C3CC46839A.

Amara, M.S., Rouzière, S., Paineau, E., Bacia-Verloop, M., Thill, A., Launois, P., 2014. Hexagonalization of aluminogermanate imogolite nanotubes organized into closed-packed bundles. J. Phys. Chem. C 118, 9299–9306.

Amara, M.S., Paineau, E., Rouzière, S., Guiose, B., Krapf, M.E.M., Taché, O., Launois, P., Thill, A., 2015. Hybrid, tunable-diameter, metal oxide nanotubes for trapping of organic molecules. Chem. Mater. 27, 1488–1494.

Bates, T.F., Hildebrand, F.A., Swineford, A., 1950. Morphology and structure of endellite and halloysite. Am. Mineral. 35, 463–484.

Belorizky, E., Fries, P.H., Guillermo, A., Poncelet, O., 2010. Almost ideal 1d water diffusion in imogolite nanotubes evidenced by nmr relaxometry. Chem. Phys. Chem. 11, 2021–2026.

Bishop, J.L., Rampe, E., Bish, D., Abidin, Z., Baker, L., Matsue, N., Henmi, T., 2011. Spectral and hydration properties of allophane and imogolite. Clay Clay Miner. 61, 57–74. https://doi.org/10.1346/CCMN.2013.0610105.

Bottero, I., Bonelli, B., Ashbrook, S., Wright, P., Zhou, W., Tagliabue, M., Armandi, M., Garrone, E., 2011. Synthesis and characterization of hybrid organic/inorganic nanotubes of the imogolite type and their behaviour towards methane adsorption. Phys. Chem. Chem. Phys. 13, 744–750. https://doi.org/10.1039/c0cp00438c.

Chagas da Silva, M., Campos dos Santos, E., Lourenco, M.P., Pereira Gouvea, M., Duarte, H.A., 2015. Structural, electronic, and mechanical properties of inner surface modified imogolite nanotubes. Front. Mater. 2, 16222–16229. https://doi.org/10.3389/fmats.2015.00016.

Chen, W., Cheng, H., Liu, Y., 2010. Radial mechanical properties of single-walled carbon nanotubes using modified molecular structure mechanics. Comput. Mater. Sci. 47, 985–993. https://doi.org/10.1016/j.commatsci.2009.11.034.

Chijioke, A.D., Nellis, W.J., Soldatov, A., Silvera, I.F., 2005. The ruby pressure standard to 150 gpa, 98, p. 114905. https://doi.org/10.1063/1.2135877.

Cradwick, P., Farmer, V., Russell, J., Masson, C., Wada, K., Yoshinaga, N., 1972. Imogolite, a hydrated aluminium silicate of tubular structure. Nat. Phys. Sci. 240, 187–189.

D'Angelo, A., Paineau, E., Rouzière, S., Elkaim, E., Goldmann, C., Toquer, D., Rols, S., Launois, P., 2023. The atomic structure of imogolite nanotubes: a 50 years old issue reinvestigated by x-ray scattering experiments and molecular dynamics simulations. Appl. Clay Sci. 242, 107043.

Elliott, J., Poli, E., Scivetti, I., Ratcliff, L., Andrinopoulos, L., Dziedzic, J., Hine, N., Mostofi, A., Skylaris, C.K., Haynes, P., Teobaldi, G., 2017. Chemically selective alternatives to photoferroelectrics for polarization-enhanced photocatalysis: the untapped potential of hybrid inorganic nanotubes. Adv. Sci. 4, 1600153.

Farmer, V.C., Fraser, A., 1979. Synthetic imogolite, a tubular hydroxyaluminium silicate. In: Developments in Sedimentology, 27. Elsevier, pp. 547–553.

Farmer, V., Fraser, A., Tait, J., 1977. Synthesis of imogolite: a tubular aluminium silicate polymer. J. Chem. Soc. Clin. Commun. 12, 462–463.

Gonzalez, R., Rogan, J., Bringa, E., Valdivia, J., 2016. Mechanical response of aluminosilicate nanotubes under compression. J. Phys. Chem. C 120, 14428–14434. https://doi.org/10.1021/acs.jpcc.6b04564.

Guimaraes, L., Enyashin, A., Frenzel, J., Heine, T., Duarte, H., Seifert, G., 2007. Imogolite nanotubes: stability, electronic, and mechanical properties. ACS Nano 1, 362–368. https://doi.org/10.1021/nn700184k.

Jimenéz-Calvo, P., Naciri, Y., Sobolewska, A., Isaacs, M., Zhang, Y., LeForestier, A., Degrouard, J., Rouzière, S., Goldmann, C., Vantelon, D., Hettler, S., Zaluzec, N., Arenal, R., Launois, P., Ghazza, M., Paineau, E., 2023. Ti-modified imogolite nanotubes as promising photocatalyst 1d nanostructures for h2 production. Small Methods, 2301369. https://doi.org/10.1002/smtd.202301369.

Kang, D.Y., Brunelli, N., Yucelen, G., Venkatasubramanian, A., Zang, J., Leisen, J., Hesketh, P., Jones, C., Nair, S., 2014. Direct synthesis of single-walled aluminosilicate nanotubes with enhanced molecular adsorption selectivity. Nat. Commun. 5, 3342. https://doi.org/10.1038/ncomms4342.

Konduri, S., Mukherjee, S., Nair, S., 2006. Strain energy minimum and vibrational properties of single-walled aluminosilicate nanotubes. Phys. Rev. B 74, 033401. https://doi.org/10.1103/PhysRevB.74.033401.

Konduri, S., Mukherjee, S., Nair, S., 2007. Controlling nanotube dimensions: Correlation between composition, diameter, and internal energy of single-walled mixed oxide nanotubes. ACS Nano 1, 393–402. https://doi.org/10.1021/nn700104e.

Krasilin, A., 2020. Energy modeling of competition between tubular and platy morphologies of chrysotile and halloysite layers. Clay Clay Miner. 68, 436–445. https://doi.org/10.1007/s42860-020-00086-6.

Lecouvet, B., Horion, J., D'Haese, C., Bailly, C., Nysten, B., 2013. Elastic modulus of halloysite nanotubes. Nanotechnology 24, 105704.

Lee, S.U., Choi, Y.C., Youm, S.G., Sohn, D., 2011. Origin of the strain energy minimum in imogolite nanotubes. J. Phys. Chem. C 115, 5226–5231. https://doi.org/10.1021/jp108629z.

Li, L., Xia, Y., Zhao, M., Song, C., Li, J., Liu, X., 2008. The electronic structure of a single-walled aluminosilicate nanotube. Nanotechnology 19, 175702. https://doi.org/10.1088/0957-4484/19/17/175702.

Liao, Y., Picot, P., Brubach, J.B., Roy, P., Le Caer, S., Thill, A., 2018. Self-supporting thin films of imogolite and imogolite-like nanotubes for infrared spectroscopy. Appl. Clay Sci. 164, 58–67. https://doi.org/10.1016/j.clay.06.005.

Liou, K.H., Tsou, N.T., Kang, D.Y., 2015. Relationships among the structural topology, bond strength, and mechanical properties of single-walled aluminosilicate nanotubes. Nanoscale 7, 16222–16229. https://doi.org/10.1039/c5nr03365a.

Liu, C.H., Kang, D.Y., 2017. Influence of interwall interaction in double-walled aluminogermanate nanotubes on mechanical properties. Comput. Mater. Sci. 135, 54–63. https://doi.org/10.1016/j.commatsci.2017.03.046.

Lourenço, M., Guimaraes, L., Da Silva, M., de Oliveira, C., Heine, H., Duarte, H., 2014. Nanotubes with well-defined structure: single and double-walled imogolites. J. Phys. Chem. C 118, 5945–5953. https://doi.org/10.1021/jp411086f.

Ma, H., Xu, J., 1994. Mean-square radius of gyration of poly(dimethylsiloxane) chain with side groups. Polym. J. 26, 779–785. https://doi.org/10.1295/polymj.26.779.

Maillet, P., Levard, C., Larquet, E., Mariet, C., Spalla, O., Menguy, N., Masion, A., Doelsch, E., Rose, J., Thill, A., 2010. Evidence of double-walled al- ge imogolite-like nanotubes. A cryo-tem and saxs investigation. J. Am. Chem. Soc. 132, 1208–1209.

Marcus, Y., 1998. The Properties of Solvents. Wiley.

Monet, G., Amara, M.S., Rouzière, S., Paineau, E., Chai, Z., Elliott, J.D., Poli, E., Liu, L.M., Teobaldi, G., Launois, P., 2018. Structural resolution of inorganic nanotubes with complex stoichiometry. Nat. Commun. 9, 1–9.

Monet, G., Paineau, E., Chai, Z., Amara, M.S., Orecchini, A., Jimenéz-Ruiz, M., Ruiz-Caridad, A., Fine, L., Rouzière, S., Liu, L.M., et al., 2020. Solid wetting-layers in inorganic nano-reactors: the water in imogolite nanotube case. Nanoscale Adv. 2, 1869–1877.

Mukherjee, S., Bartlow, V., Nair, S., 2005. Phenomenology of the growth of single-walled aluminosilicate and aluminogermanate nanotubes of precise dimensions. Chem. Mater. 17, 4900–4909.

Ookawa, M., Hirao, Y., Watanabe, M., Maekawa, T., Inukai, K., Miyamoto, S., Yamagushi, T., 2006. Synthesis of aluminum germanate tubular material using germanium oxide as the source of germanium. Clay Sci. 13, 69–73. https://doi.org/10.11362/jcssjclayscience1960.13.69.

Paineau, E., Amara, M., Monet, G., Peyre, V., Rouzière, S., Launois, P., 2017. Effect of ionic strength on the bundling of metal oxide imogolite nanotubes. J. Phys. Chem. C 121, 21740–21749.

Park, G., Lee, H., Lee, S., Sohn, D., 2014. Strain energy and structural property of methyl substituted imogolite. Mol. Cryst. Liq. Cryst. 599, 68–71. https://doi.org/10.1080/15421406.2014.935924.

Patra, S., Testard, F., Gobeaux, F., Sicard, L., Shaming, D., Le Caër, S., Thill, A., 2023. Uv-visible photo-reactivity of permanently polarized inorganic nanotubes coupled to gold nanoparticles. Nanoscale 15, 4101–4113. https://doi.org/10.1039/D2NR05796D.

Pebdani, M.H., 2023. Molecular insight into structural and mechanical properties of halloysite structure. Comput. Mater. Sci. 218, 111948.

Piperno, S., Kaplan-Ashiri, I., Cohen, S., Popovitz-Biro, R., Wagner, H., Tenne, R., Foresti, E., Lesci, I., Roveri, N., 2007. Characterization of geoinspired and synthetic chrysotile nanotubes by atomic force microscopy and transmission electron microscopy. Adv. Funct. Mater. 17, 3332–3338. https://doi.org/10.1002/adfm.200700278.

Robertson, D.H., Brenner, D.W., Mintmire, J.W., 1992. Ener getics of nanoscale graphitic tubules. Phys. Rev. B 45, 12592. https://doi.org/10.1103/PhysRevB.45.12592.

Rouzière, S., Balédent, V., Paineau, E., Elkaim, E., Bizien, T., Nataf, L., Pan, Y., Launois, P., 2023. Compressibility and structural transformations of aluminogermanate imogolite nanotubes under hydrostratic pressure. Inorg. Chem. 62, 957–966.

Salvetat, J.P., Briggs, G., Bonard, J.M., Bacsa, R., Kulik, A., Stöckli, T., Burnham, N., Forró, L., 1999. Elastic and shear moduli of single-walled carbon nanotube ropes. Phys. Rev. Lett. 82, 944. https://doi.org/10.1103/PhysRevLett.82.944.

San Miguel, A., 2006. Nanomaterials under high-pressure. Chem. Soc. Rev. 35, 876–889. https://doi.org/10.1039/b517779k.

Serra, M., Arenal, R., Tenne, R., 2019. An overview of the recent advances in inorganic nanotubes. Nanoscale 11, 8073–8090. https://doi.org/10.1039/C9NR01880H.

Tateiwa, N., Haga, Y., 2009. Evaluations of pressure-transmitting media for cryogenic experiments with diamond anvil cell. Rev. Sci. Instrum. 80, 1–9. https://doi.org/10.1063/1.3265992.

Teobaldi, G., Beglitis, N.S., Fisher, A.J., Zerbetto, F., Hofer, W.A., 2009. Hydroxyl vacancies in single-walled aluminosilicate and aluminogermanate nanotubes. J. Phys. Condens. Matter 21, 195301.

Thill, A., Guiose, B., Bacia-Verloop, M., Geetsen, V., Belloni, L., 2012. How the diameter and structure of (oh)3al2o3sixge1xoh imogolite nanotubes are controlled by an adhesion versus curvature competition. J. Phys. Chem. C 116, 26841–26849. https://doi.org/10.1021/jp310547k.

Wada, S.I., Wada, K., 1982. Effects on substitution of germanium for silicon in imogolite. Clay Clay Miner. 30, 123–128. https://doi.org/10.1346/ccmn.1982.0300206.

Whittaker, E., 1956. The structure of chrysotile. II. Clino-chrysotile. Acta Crystallogr. 9, 855–862. https://doi.org/10.1107/S0365110X5600245X.

Yoshinaga, N., Aomine, S., 1962. Imogolite in some ando soils. Soil Sci. Plant Nutr. 8, 22–29.

Zanzottera, C., Armandi, M., Esposito, S., Garrone, E., Bonelli, B., 2012a. Co2 adsorption on aluminosilicate single-walled nanotubes of imogolite type. J. Phys. Chem. C 116, 7499–7506. https://doi.org/10.1021/jp3061637.

Zanzottera, C., Vicente, A., Armandi, M., Fernandez, C., Garrone, E., Bonelli, B., 2012b. Thermal collapse of single-walled aluminosilicate nanotubes: transformation mechanisms and morphology of the resulting lamellar phases. J. Phys. Chem. C 116, 23577–23584. https://doi.org/10.1021/jp3090638.

Zhang, J., Yang, L., Wu, X., Wei, M., Liu, Y., Gao, C., Yang, J., Ma, Y., 2018. Correlation between structural change and electrical transport properties of fe-doped chrysotile nanotubes under high pressure. J. Phys. Condens. Matter 30, 144008–144014. https://doi.org/10.1088/1361-648X/aab392.